iScience

CellPress
OPEN ACCESS

Article

Three-point bending damage detection of GFRP composites doped with graphene oxide by acoustic emission technology

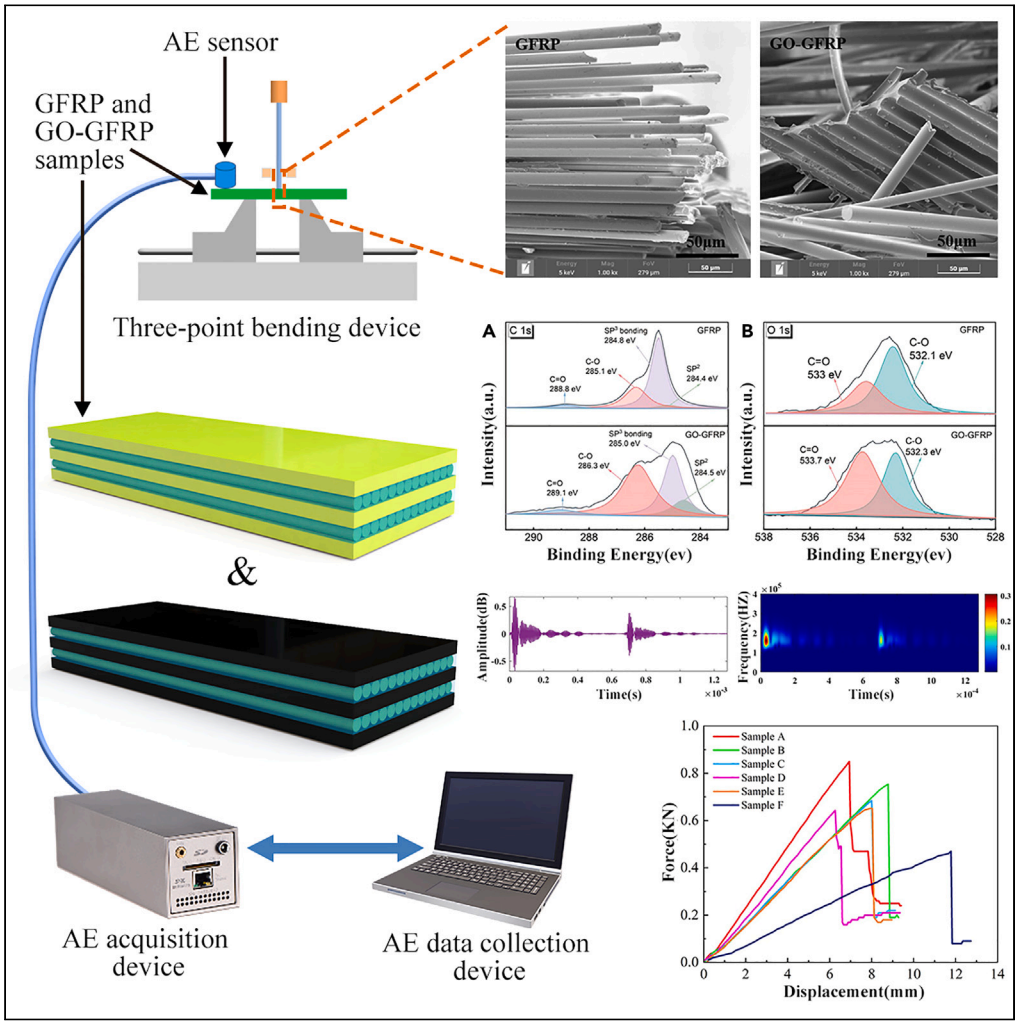

Wangyong Shu, Lida Liao, Pengzhan Zhou, Bin Huang, Weike Chen

lidaliao@csust.edu.cn

Highlights

This study investigated the damage mechanisms of GO-GFRP and GFRP composites

Sentery function showed the main distinction between GO-GFRP and GFRP was in stage ii

The AE signals were analyzed using MVMD and the generalized S transform

Compared to GFRP, GO-GFRP is more prone to fiber debonding

Shu et al., iScience 26, 108511
December 15, 2023
https://doi.org/10.1016/j.isci.2023.108511

iScience

CellPress
OPEN ACCESS

Article

Three-point bending damage detection of GFRP composites doped with graphene oxide by acoustic emission technology

Wangyong Shu,[1] Lida Liao,[1,3,*] Pengzhan Zhou,[1] Bin Huang,[1,2] and Weike Chen[1]

SUMMARY

The incorporation of graphene oxide (GO) into composite materials can modulate their overall performance. To enhance the performance of acoustic emission (AE) signals, 3% GO was incorporated into glass fiber-reinforced polymer (GFRP) composites, resulting in the creation of GO-GFRP composite materials. The sentry function was first used to investigate the damage evolution of the material. Then, the AE signals were analyzed using multivariate mode decomposition (MVMD) and the generalized S transform to identify the damage mechanisms. Finally, scanning electron microscopy (SEM) was used to observe the fracture surfaces of the samples to confirm the material failure. The experiments identified four damage mechanisms: matrix cracking, fiber debonding, delamination failure, and fiber breakage. It was also found that GO-GFRP composites are more prone to fiber debonding compared to GFRP composites without added GO.

INTRODUCTION

Glass fiber–reinforced polymer (GFRP) composites, as an advanced composite material, has an excellent strength, corrosion resistance, fatigue resistance, and molding processability.[1] It is widely used in industries such as the construction, aerospace, automotive, shipbuilding, and wind power generation industries.[2–4] Consequently, a considerable number of studies[5–7] have researched the improvement of GFRP material properties.

Graphene can improve the physical, chemical, and mechanical properties of materials.[8] Graphene oxide (GO), as a derivative of graphene,[9] makes it suitable for improving the performance of GFRP composites. Fu et al.[10] described research on the use of GO-modified polymer composites in a literature review, including improvements in the mechanical, electrical, electrochemical, thermal, adsorption, barrier, and other properties. Chen et al.[11] improved the heat transfer performances and efficiencies of glass fiber/epoxy resin (GF/EP)–reinforced polymer composites by doping them with GO, and the composites were used for anti-icing applications. Finally, Zhao et al.[12] adjusted the interfacial and interlaminar properties of glass-fiber fabric/epoxy laminated composites by adding GO with different oxidation degrees. In current research, modification of the mechanical properties of GFRP composites is typically achieved by adding GO. This study, however, focuses on modifying the damage evolution process of GFRP materials by incorporating GO through acoustic emission (AE) detection.

To prevent safety incidents caused by damage in the actual application of GFRP composites, monitoring techniques for the integrity and health of the material structure are of widespread interest. Fausto Pedro García Márquez and Ana María Peco Chacón discussed various nondestructive testing (NDT) methods for wind turbine blades in their literature review,[13] including visual inspection, shear imaging, thermal imaging, ultrasonic testing, radiographic testing, electromagnetic testing (ET), and AE testing. AE can effectively monitor the microscopic structural changes or internal damage evolution of composite materials.[14] When a material or structure is subjected to external loads or internal stresses, such as during mechanical loading, fatigue cycles, or temperature changes, it may cause minor displacements and strains. These minor changes can lead to the expansion of micro-cracks or the formation of other damage in the material. When these cracks form or damage occurs, they generate high-frequency sound wave signals, which can be captured and analyzed by an AE detection system.

In the monitoring of composite materials, AE testing is widely used to identify the damage types in GFRP composites, including matrix cracking, fiber debonding, delamination, and fiber fracture. Each type of damage generates characteristic AE signals. Jung et al.[15] used AE to detect damage in carbon fiber–reinforced polymer (CFRP) composites and applied the Cb-value to analyze the AE amplitude distribution at the origin of the crack in the composite. The Cb-value is calculated based on data from various sensor locations and provides accurate information about the overall damage state. Friedrich et al.[16] used the b-value to describe the statistical characteristics of signal amplitude, and then used the c-value and frequency fluctuations to characterize the frequency features of the signal, thereby analyzing the damage evolution process in GFRP composites. In other studies,[17,18] b-values and improved b-values (Ib-values, which are calculated based on the

[1]School of Energy and Power Engineering, Changsha University of Science and Technology, Changsha, Hunan Province 410114, China
[2]UniSA STEM, University of South Australia, Adelaide, SA 5095, Australia
[3]Lead contact
*Correspondence: lidaliao@csust.edu.cn
https://doi.org/10.1016/j.isci.2023.108511

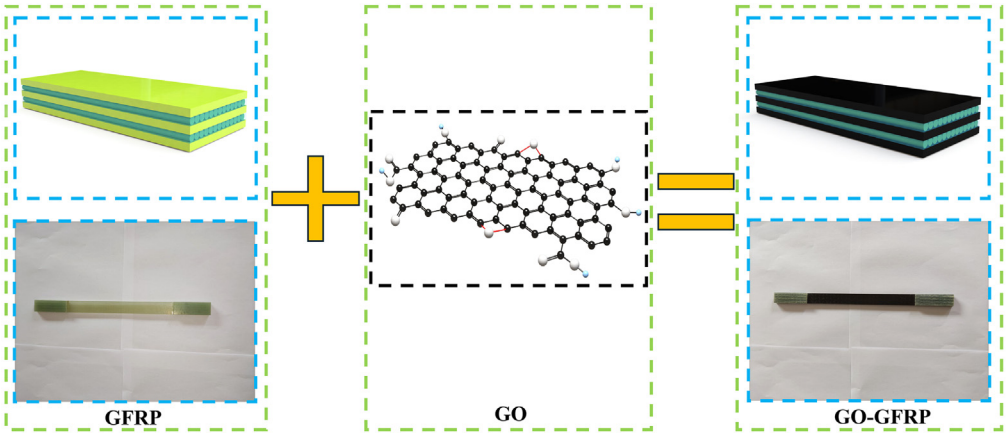

Figure 1. Schematic diagram of the samples

mean and standard deviation of the AE signal amplitude distribution) have been employed in AE damage evolution analysis for damage detection in composite materials. Wang et al.[19] used the sentry function and short-time Fourier transform (STFT) to analyze the damage process and signals in ceramic matrix composites with three-dimensional braided structures (3D_C/C_TiC_Cu).

Various studies have examined analysis methods for the characteristic signals in AE. Zhang et al.[20] applied principal component analysis (PCA) and k-means clustering to identify material damage signals in AE signal processing. Harizi et al.[21] further identified GFRP composite damage signals through the coupling of PCA, k-means clustering, and a Kohonen self-organizing map (KSOM). Mi et al.[22] analyzed the AE signals of GFRP composites under tension through a wavelet transform and the fuzzy C-Means method (FCM). Azadi et al.[23] studied the damage mechanism of open-hole carbon fiber–reinforced polymer composites under tension using the wavelet packet transform (WPT) and FCM. Chelliah et al.[24] conducted a comparative study of AE signal feature classification techniques for GFRP composites using k-means, FCM clustering, and a KSOM, finding that both the FCM and KSOM methods had high reliability. Beheshtizadeh et al.[25] employed a wavelet transform and Choi–Williams transform to analyze AE signals and study the damage mechanism of glass fiber–epoxy resin composites.

In this study, AE technology was employed to study the damage evolution process and damage mechanism of GFRP composites under bending stress, and the impact of GO addition on the damage mechanism of glass fiber was explored using 3% GO. Two different types of samples were used during the experimental process, and three-point bending damage control tests were conducted at different rates. The impact of GO on the GFRP composites damage under bending stress was characterized using AE technology. To validate the damage mechanism, scanning electron microscopy (SEM) was employed to photograph the samples at the microscopic level after the experiments, serving as a supplementary method for verification. Data processing and analysis were conducted using MATLAB software; the relationship between the bending stress damage changes and AE signals was studied using the sentry function to determine the material's damage evolution process. Subsequently, the generalized S transform was used to analyze the time–frequency features of AE signals at different stages of three-point bending damage in the GFRP composites.

Acoustic emission signal processing methodology

Sentry function

The sentinel function combines the cumulative energy of the AE with the mechanical energy,[25] and it is the only method that directly connects the AE with the load.[26] During the process of external force loading, materials release the strain energy stored internally due to internal failure. The signal energy is the primary form of energy release from the material.[13] The formula is as follows:

$$f(x) = \ln\left[\frac{E_{SE}(x)}{E_{AE}(x)}\right], \quad \text{(Equation 1)}$$

where E_{SE} represents the mechanical strain energy, E_{AE} represents the accumulated AE energy, and x represents the displacement or strain. The mechanical energy E_{SE} is obtained by computing the area under the stress (Y axis) vs. displacement (X axis) curve. The sentinel function value obtained from the correlation between the mechanical energy and accumulated AE energy can monitor the mechanical damage process of the test piece. During the experiment, the test can be stopped if the specimen does not produce any AE signals or is in a state of complete failure during the mechanical test. The sentinel function may be discontinuous. Discontinuity of the sentinel function values has been found both in the study of glass fiber-epoxy resin composites[25] and in the research of carbon fiber-epoxy resin composites.[26]

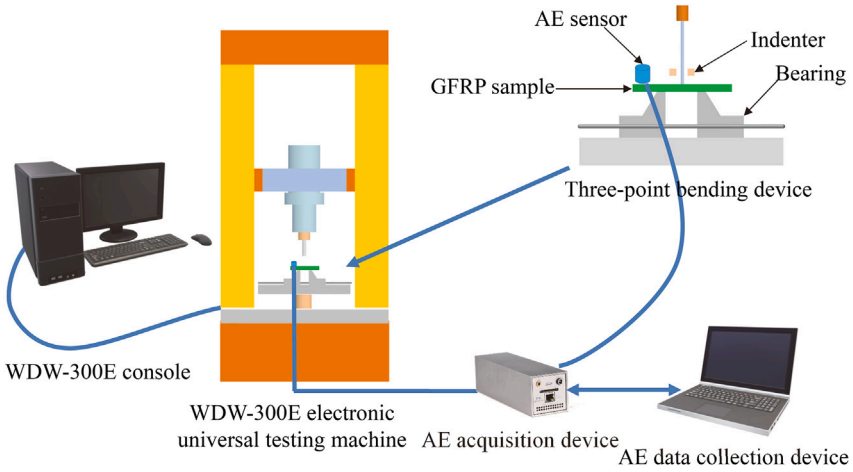

Figure 2. Schematic diagram of the experimental setup

Multivariate variational mode decomposition

MVMD,[27] as an improvement and extension of variational mode decomposition (VMD),[28] serves as a decomposition method for nonstationary signals, primarily used for filtering, denoising, and feature extraction of AE signals. The equation for the MVMD method is as follows:

$$X(t) = \sum_{k=1}^{K} a_k(t), \quad \text{(Equation 2)}$$

where K is the number of modes to be decomposed, and each decomposed mode is obtained.

Generalized S transform

The S transform proposed by Stockwell et al.[29] is an improved method based on the shortcomings of the wavelet transform (WT) and short-time Fourier transform (STFT). Compared to the STFT, the S transform has the advantage of using a Gaussian function with a nonfixed variance. The S transform is defined as follows:

$$S(\tau, F) = \int_{-\infty}^{\infty} x(t)\omega(\tau - T, F)e^{(-2\pi iFT)}dT, \quad \text{(Equation 3)}$$

$$\omega(\tau - T, F) = \frac{|F|}{\sqrt{2\pi}}e^{\frac{-(T-\tau)^2F^2}{2}}, \quad \text{(Equation 4)}$$

Where F is the frequency, T is the time, $\omega(\tau - T, F)$ is the Gaussian window function, τ controls the position of the Gaussian window on the time axis (T), and i is the imaginary unit.

In the analysis of the time–frequency spectrum of the AE in GFRP composites, the S transform has the advantage of a high resolution. The generalized S transform is an extension of the S transform method, which, by introducing adjustable parameters, offers a more flexible approach to handle nonstationary signal time–frequency analysis. The calculation method of the generalized S transform is to convolve the signal with window functions of different scales and shapes. By making appropriate adjustments in the time and frequency domains, the signal can be represented on the time–frequency plane, showing the local characteristics of the signal at different times and frequencies. The expression of the generalized S transform is as follows:

$$S(\tau, F) = \int_{-\infty}^{\infty} x(t)\omega(\tau - T, F)e^{(-2\pi iFT)}dT, \quad \text{(Equation 5)}$$

Table 1. Acoustic emission (AE) system parameter settings

AE Acquisition Parameter Settings		AE Timing Parameter Settings		
Threshold	Sampling rate	PDT	HDT	HLT
55 dB	1.25 MSPS	100 μs	200 μs	300 μs

HDT, impact definition time; HLT, impact lock time; PDT, peak definition time.

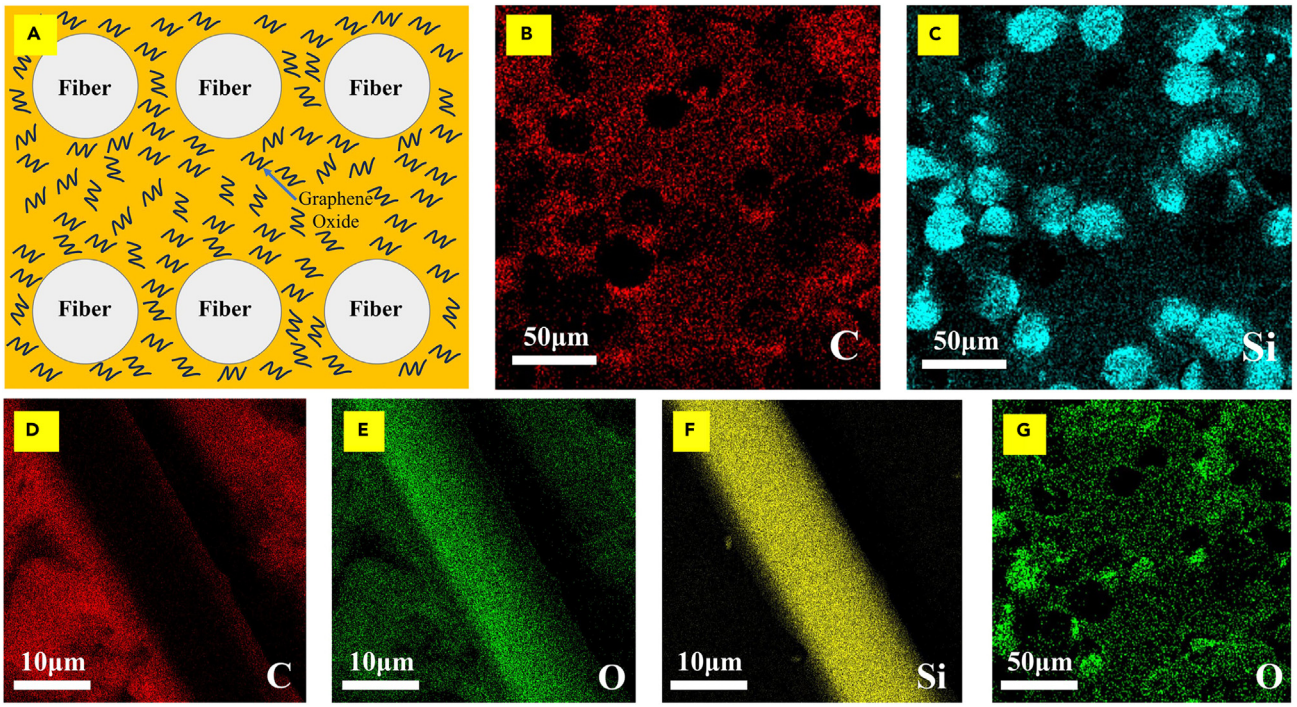

Figure 3. Distributions of C, O, and Si determined by energy-dispersive X-ray spectroscopy (EDS) in the material

(A) Schematic diagram of GO distribution in GFRP samples.

(B–G) EDS mapping images show the composition and distribution of C, O, and Si in the samples.

$$\omega(\tau - T, F) = \frac{\lambda|F|^p}{\sqrt{2\pi}} e^{\frac{-\lambda^2 F^2 p (T-\tau)^2}{2}}, \quad \text{(Equation 6)}$$

where $\lambda > 0$, $p > 0$ (when $\lambda = 1$, $p = 1$, it is the standard S transform; when $\lambda > 1$, the width of the time window inversely changes with the speed of the signal frequency; and when $\lambda < 1$, the time window width decreases inversely with the speed of signal frequency transformation.

Experiment

Experimental materials

The experimental materials were prepared using a method of double-layer flat laying with unidirectional glass fibers at 0^0. First, a unidirectional glass-fiber cloth was laid on a flat mold, and then it was heated and pressurized in an oven to cure, resulting in a composite laminate. This process was repeated to finally obtain a two-layer unidirectional glass fiber/epoxy resin–reinforced composite material, as shown in Figure 1. The epoxy resin with the added curing agent was dried and cured by heating with a 101-type electric blast drying oven, and after

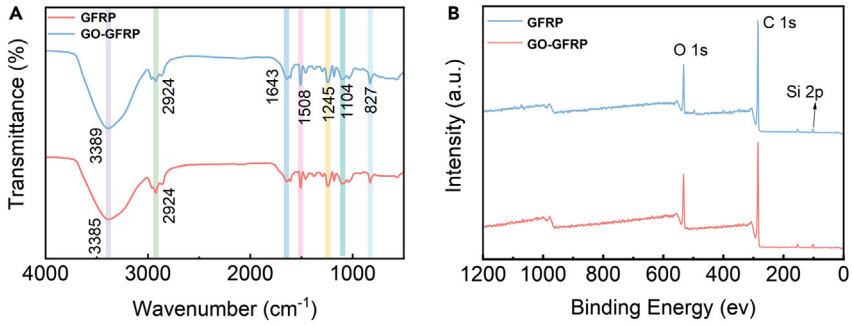

Figure 4. FTIR and XPS spectra graphs of GFRP and GO-GFRP samples

(A) FTIR spectra graph of GFRP and GO-GFRP samples.

(B) XPS spectra graph of GFRP and GO-GFRP samples.

Table 2. Relative surface element contents of samples

Sample	C	O
GFRP	82.98	13.87
GO-GFRP	84.19	14.26

GFRP, glass fiber–reinforced polymer; GO, graphene oxide.

cooling, a 300 mm × 250 mm GFRP composite pressure plate containing GO was obtained. The mixture contained 100 g of epoxy resin, 34 g of curing agent, and 5 g of GO, and it was evenly mixed through mechanical stirring. The total mass of the resulting composite pressure plate was 150 g, with GO accounting for 3% of this mass. Finally, in order to reduce the internal damage to the specimens during the cutting process and to prevent the generation of a large amount of heat during the cutting process from affecting or even burning the specimens, a water cutting method was used to cut the GFRP composite pressure plate. According to the GB/T 3356-2014 standard, the GFRP composite was cut into test specimens with dimensions of 250 mm × 16 mm × 3 mm. Later in discussion are the schematic diagrams of the GFRP samples and the GFRP samples with added GO (GO-GFRP), as shown in Figure 1.

Experimental equipment and testing procedures

Three-point bending tests were carried out using a WDW-300E electronic universal testing machine. The experimental method was conducted according to the GB/T 3356-2014 standard. As shown in Figure 2, three identical samples were grouped and subjected to repeated bending tests at loading rates of 5, 7.5, and 10 mm/min, with a span of 60 mm. AE data was collected using an AE data acquisition device developed and produced by Changsha Pengxiang Electronic Technology Co., Ltd. The sensor used was the pxR15 resonant sensor. In order to verify the sensitivity of the AE system, a lead break measurement was required before the start of the experiment. Markings were made at distances of 3 cm, 5 cm, and 7 cm; intervals of 2 cm from the middle of the specimen where the bending force was applied. The amplitude exhibited a decreasing trend, but all were above 80 dB, meeting the test requirements. The AE signals during the process were not interfered with by environmental noise. The collected parameters are shown in Table 1, where PDT refers to the peak definition time, HDT refers to the impact definition time, and HLT refers to the impact lock time.

RESULTS AND DISCUSSION

Material structure

With the aid of various material analysis techniques such as energy dispersive X-ray spectroscopy (EDS), Fourier transform infrared spectroscopy (FTIR), and X-ray photoelectron spectroscopy (XPS), the elements and chemical properties of the material were analyzed. In the EDS analysis results shown in Figure 3, we can observe the distribution of various elements in the material. Si corresponded to the fiber bundle, while the C and O corresponded to the GO and epoxy resin. Although GO was mainly composed of C and O atoms, the epoxy resin was also primarily composed of these elements. Hence, relying solely on EDS analysis would not accurately determine whether the material contained GO. However, the distribution of GO can be observed in Figure 3.

The chemical functional groups of the GO-GFRP and GFRP samples were studied through Fourier transform infrared spectroscopy (FT-IR), as shown in Figure 4A. The diffraction peaks of GO-GFRP samples coincided with the transmission peaks of GFRP samples, indicating that the addition of a suitable amount of GO did not affect the types of surface functional groups of the glass-fiber epoxy

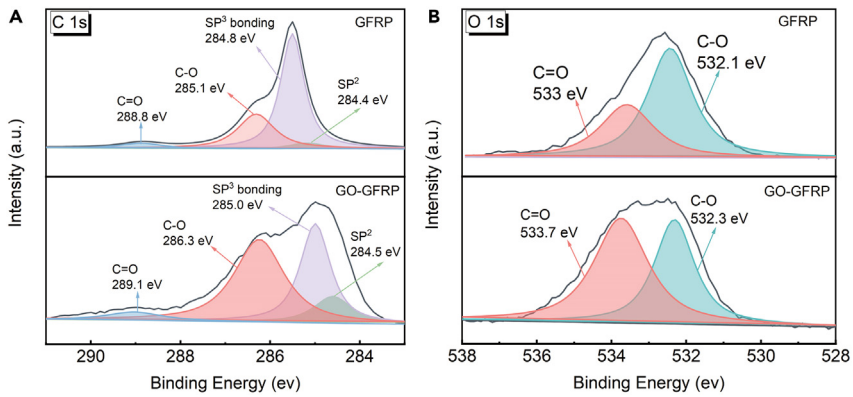

Figure 5. XPS C1s and XPS O1s spectra of GO-GFRP and GFRP samples

(A) XPS C1s spectra of GO-GFRP and GFRP samples.

(B) XPS O1s spectra of GO-GFRP and GFRP samples.

Table 3. Fitted peak components (in%) of C1s and O1s for GO-GFRP and GFRP samples using XPS curve fitting

	C1s			O1s	
Sample	C-C or C-H	C-O	C=O	C=O	C-O
GFRP	51.28	43.18	5.54	69.61	30.39
GO/GFPR	71.22	24.79	3.99	45.91	54.09

GFRP, glass fiber–reinforced polymer; GO, graphene oxide; XPS, X-ray photoelectron spectroscopy.

resin. In comparison with GFRP sample's absorption peak at 3389 cm^{-1}, a red shift in the absorption peak of the GO-GFRP sample was observed at 3385 cm^{-1}, indicating that -OH stretching was affected by the doping of GO. A distinct characteristic peak appeared near 2924 cm^{-1}, possibly representing the C—H stretching vibrations of saturated carbon. The peaks at 1643 and 1508 cm^{-1} were related to the stretching vibrations of benzene rings. The peak at 1245 cm^{-1} suggested the presence of ether bond stretching vibrations in aromatic and aliphatic compounds. The characteristic peak at 1104 cm^{-1} corresponded to the C-O-C functional groups in the epoxy resin, while the peak at 827 cm^{-1} corresponded to the bending vibrations between adjacent hydrogen atoms on a para-substituted benzene ring.

To further determine the differences between these two materials, we used XPS to analyze the GFRP and GO-GFRP samples. Figure 4B shows the results of the elemental spectrum analysis, where the peaks at 101.4, 286.4, and 534.4 eV corresponded to Si2p, C1s, and O1s, respectively. According to the data in Table 2, the carbon and oxygen contents in the GO-GFRP samples were higher than those in the GFRP samples. By using the XPSPEAK software to perform peak fitting of the carbon and oxygen signals of the GFRP and GO-GFRP samples (as shown in Figure 5), we obtained the following results. For the GFRP sample, the characteristic peaks at 284.5, 285, 286.3, and 289.1 eV corresponded to GFRP sample's C-C sp2 bonds, C-C sp3 bonds, epoxy resin and epoxy group C-O, and C=O groups. The peaks at the binding energies of 532.3 and 533.7 eV represent the C=O and C-O groups, respectively. According to the data in Table 3, the carbon content in the GO-GFRP sample increased from 82.98% to 84.19% after the addition of GO. In addition, regarding the composition of oxygen-containing functional groups, the peak intensity of the C=O functional groups in the GO-GFRP sample was lower, indicating that the GO-GFRP sample was well oxidized and the surface oxygen-containing functional groups were rich. Compared to the GFRP sample, the C=O and C-O peaks of the GO-GFRP sample had shifted, indicating that after the addition of epoxy resin, the chemical environment after the graphene and epoxy resin compositing had changed.

Mechanical damage analysis

Mechanical test results

The GFRP and GO-GFRP samples were divided into six groups, labeled A, B, C, D, E, and F, for three-point bending analysis. Figure 6 displays the stress-displacement curves of these samples. Samples A–C were GFRP samples, while samples D–F were GO-GFRP samples. The bending rates for samples A and D were 5 mm/min, those of samples B and E were 7.5 mm/min, and those of samples C and F were 10 mm/min. In the initial stage before the specimens underwent plastic deformation, the stress almost continuously showed a linear increase.

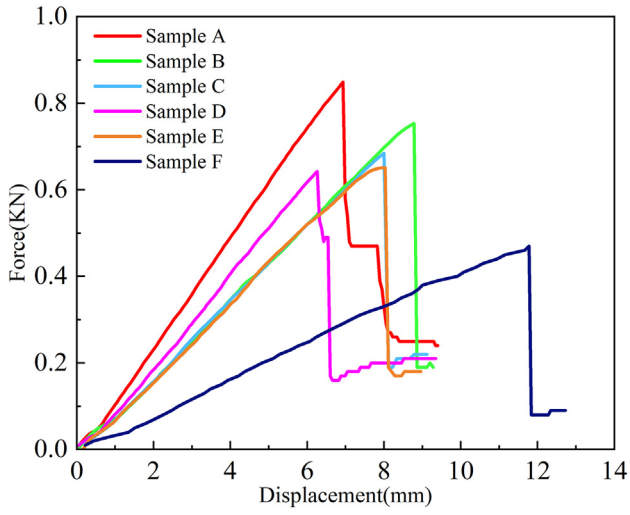

Figure 6. Mechanical testing results of the samples

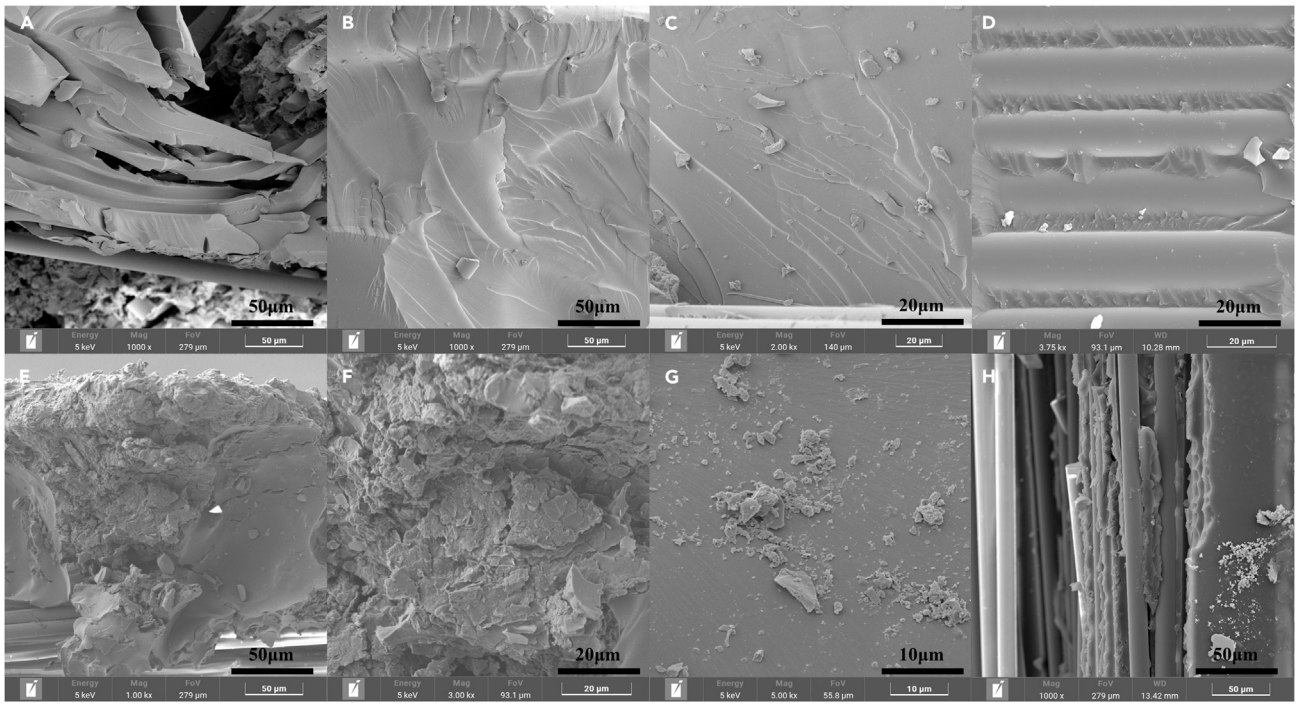

Figure 7. SEM images of the matrix in GFRP and GO-GFRP samples

(A–D) Characteristic images of GFRP samples.

(E–H) Characteristic images of GO-GFRP samples.

Sample A reached its maximum bending limit at a displacement of 6.93 mm, with a peak load of 0.85 kN. The material failure of sample D occurred at a displacement of 6.26 mm, with a peak load of 0.64 kN. Sample B reached a peak load of 0.75 kN, with a maximum displacement of 8.78 mm. Sample E had a peak load of 0.65 kN, with a maximum displacement of 8.03 mm. Samples C and F had peak loads of 0.68 kN and 0.47 kN, with maximum displacements of 8.00 mm and 11.78 mm, respectively. Mechanical testing revealed a decrease in the bending performance of GO-GFRP samples when the GO content was 3%.

Scanning electron microscopy image analysis

Damage occurred in the GFRP and GO-GFRP samples under bending stress. In the case of bending damage, damage features such as matrix cracking, fiber–matrix interface debonding, delamination, and fiber breakage should occur. In order to further understand the material's damage types, as well as the material's characteristics, SEM photographic analysis of the fracture was performed for verification. After the three-point bending test, the specimens were subjected to microscopic verification analysis using SEM.

By comparing the results in Figure 7, we can observe that there was a difference in the matrix conditions of the GO-added GFRP and regular GFRP samples before and after bending stress damage. Figures 7D and 7H show the matrix images before damage, while the other images show the situation after damage. Upon close examination of Figure 7, it can be clearly seen that there was a significant difference in the matrices of the GO-added GFRP samples and the regular GFRP samples. Compared to the GFRP samples, the GO-GFRP samples were softer and more elastic. The above images indicate that this was also a major reason for the decrease in the bending mechanical properties of the matrix.

The images of the damage features in Figure 8 reveal the different behaviors of the GFRP and GO-GFRP samples under three-point bending. In Figures 8A and 8E, the yellow markers indicate matrix cracking, which is one of the main forms of shear force damage. At the interface where stress was transferred, bending stress produced friction bending stress and bonding stress. Under the influence of stress, the specimen first exhibited a wrinkling phenomenon, which is marked in green in Figures 8B and 8F. As the stress load continued, the matrix continued to bend, leading to matrix cracking. Under normal circumstances, the damage energy of the epoxy resin was lower. However, under the interference of environmental noise, the set threshold value could not only filter out noise but could also lead to the inability to detect this part of the AE signal. After the matrix cracked, the crack extended under the influence of continuous loads, leading to fiber debonding, which is indicated in blue in Figure 8. Figure 8H shows the situation where the fiber/epoxy resin was completely debonded. In addition, the orange markers in Figure 8 show the phenomenon of delamination damage. When the laminated plate withstood tremendous stress, the matrix cracks extended to the interlayer area, and the crack tip area underwent stress concentration and structural mutation, leading to a

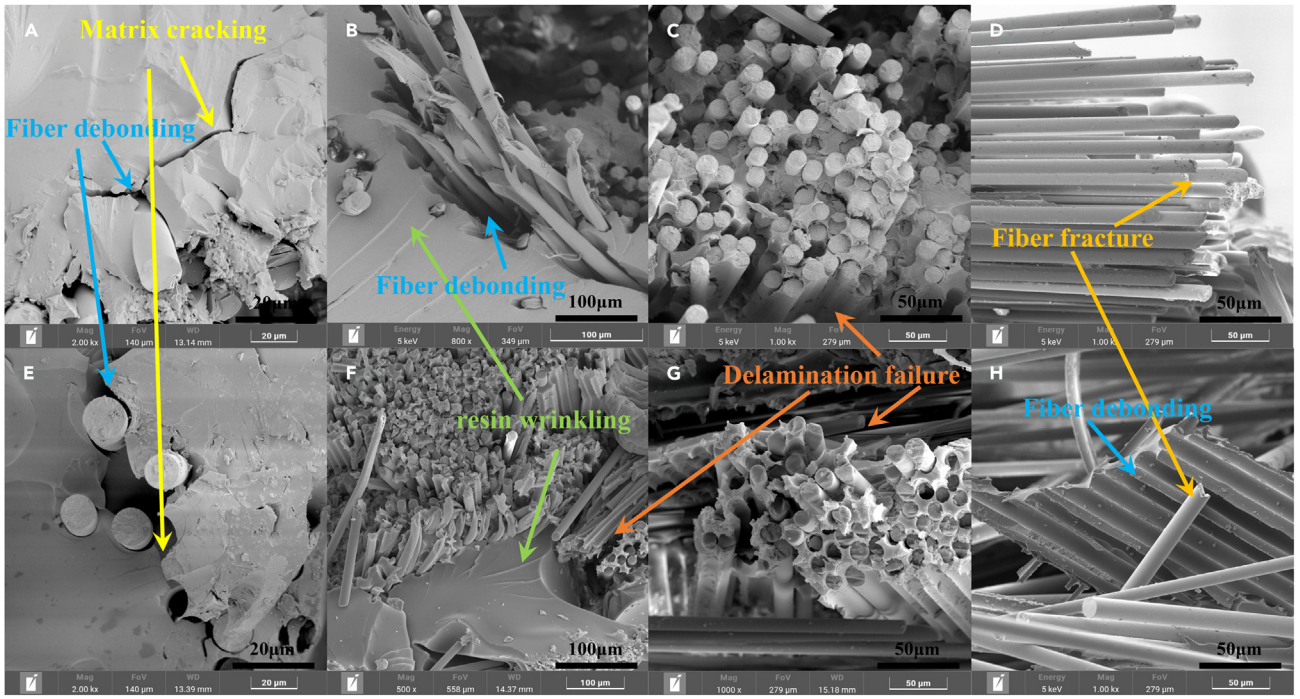

Figure 8. SEM damage images of GFRP and GO-GFRP samples

(A–D) Scanning electron microscopy (SEM) images of damage features in GFRP samples.

(E–H) SEM images of damage features in GO-GFRP samples.

drastic change in stress, causing interlaminar fractures between adjacent layers of fibers and a delamination phenomenon. Figures 8D and 8H show typical fiber fractures in the orange-yellow marked areas.

Sentry function

The evolution of damage in the specimen was examined using a sentry function, which allowed the stress damage and AE to be detected and correlated. AE detection of the damage evolution process in the specimen was performed. Figures 9A–9C are GFRP samples, and Figures 9D–9F are GO-GFRP samples.

Stage i is the stable phase of stress loading, and it is characterized by an almost linear increase in stress. The specimen initially undergoes an elastic deformation phase during this stage, and no AE signals are generated. Subsequently, as bending stress continues to be applied, microcracks appear in the specimen. According to the experimental data, the number of AE signals is relatively small in this stage, indicating that the material releases a small amount of energy in the form of signals. However, there is a slight increase in mechanical energy, resulting in a significant decrease in the sentinel function value. In this stage, there is a significant time gap between the AE signals observed in the specimen; this may be influenced by noise and the presence of a small number of cracks inside the material during the initial stage of bending stress loading, leading to a relatively small number of AE signals.

Stage ii involves a continued stable growth in stress, with the specimen remaining intact. AE signals become more active and high-energy signals start to appear, with high-energy signal growth being intermittent rather than continuous. This indicates that in the first stage, microcracks in the specimen extended to form macroscopic cracks. The sentinel function value remains relatively stable in this stage, with no significant increase in amplitude, as the cumulative AE energy increases alongside the mechanical energy. As shown in Figure 9F, the sentinel function value exhibits an increasing trend in this stage, mainly due to a smaller relative increase in cumulative energy as the mechanical energy in the specimen increases. By comparing Figures 9A and 9D, Figures 9B and 9E, and Figures 9C and 9F, noticeable differences can be observed between the GO-GFRP and GFRP samples in this stage; most notably, the GO-GFRP samples enter this stage earlier and stay in it longer.

Stage iii is the stress mutation stage, during which severe deformation occurs as a result of cumulative damage from stages i and ii. It can be seen from Figure 9 that each stress mutation point causes a discontinuity in the sentinel function value, and at each position at which the sentinel function value decreases, high-energy AE characteristic signals are present. Compared to the first two stages, the energy of AE signals in this stage exhibits an exponential increase. When the stress suddenly changes, the rate of the increase in mechanical energy decreases, leading to a sharp decrease in the sentinel function value. In Figures 9B, 9C, 9E, and 9F, before a stress mutation occurs in the specimen, the sentinel function value begins to decrease, indicating that the material experienced significant damage before the stress mutation.

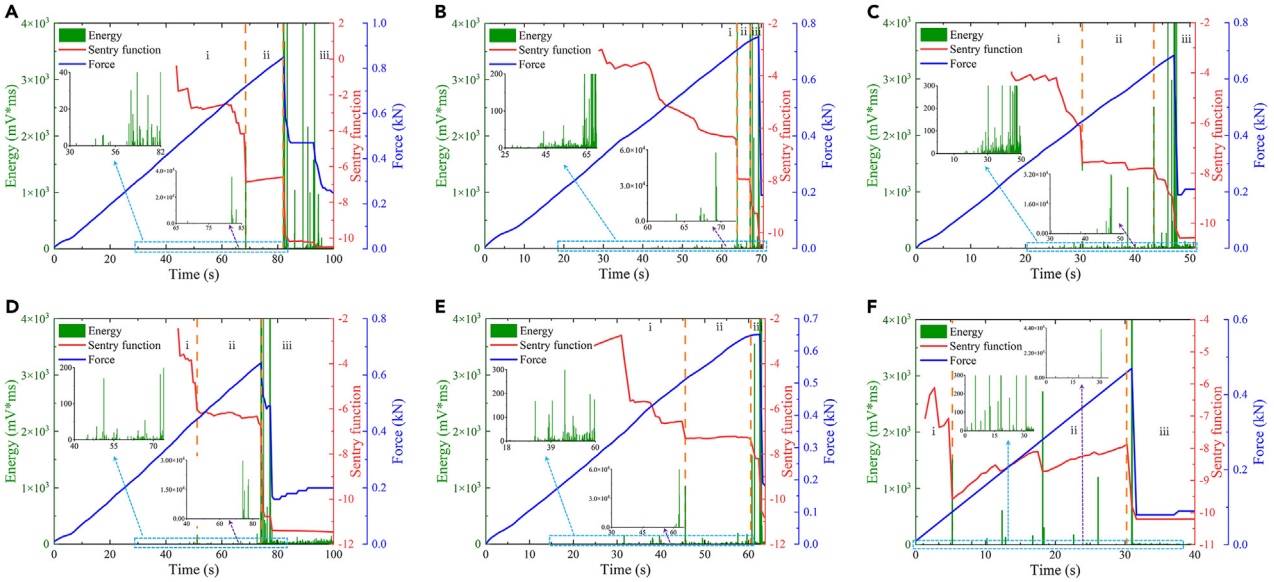

Figure 9. Correlation of the sentry function with the acoustic emission (AE) signals

(A) Sample A.

(B) Sample B.

(C) Sample C.

(D) Sample D.

(E) Sample E.

(F) Sample F.

Subsequent stress mutations result in specimen failure (in Figure 9, each drop in the sentinel function value indicates significant damage inside the specimen).

Acoustic emission signal analysis

Following the study of the material damage evolution process in the previous section, in order to further understand the damage mechanism of the material in the different stages, we used MVMD and the generalized S transform to analyze the signal damage types in stages i, ii, and iii. First, we used the MVMD method to preprocess the signal and obtain the time-domain signal after decomposition in order to reduce the impact of noise and extract the characteristic signals. However, the amplitude alone could not accurately determine the type of damage. Based on the frequency ranges corresponding to damage in the literature,[25,30,31] the generalized S transform was used to perform time–frequency analysis on the signals at different stages in order to further obtain the damage evolution mechanism within.

Figure 10 shows the signals produced by the GO-GFRP and GFRP samples in stage i. The signal frequencies of these two types of specimens were mainly concentrated in the range of 100–200 kHz. The maximum voltage values of Signal1 and Signal2 were 0.05 and 0.06 V, respectively, and those of Signal3 and Signal4 were 0.02 and 0.05 V, respectively. Within this frequency range and at these voltage values, there was a clear correlation between the signals and the damage characteristics of the specimens, which mainly manifested as matrix cracking. The SEM image of the GO-GFRP sample's matrix cracking is shown in Figure 10A, while the SEM image of the GFRP sample's matrix cracking is shown in Figure 10B. Signal1 and Signal2 are two different characteristic signals from the GO-GFRP samples in stage i, and Signal3 and Signal4 are two different characteristic signals from the GFRP samples in stage i. The amplitudes of these four groups of signals can be observed from the time–domain diagram to not exceed 0.2 dB. In addition, compared with the GFRP samples, the matrix cracking signals generated by the GO-GFRP samples in stage i had a shorter duration.

In the previous section, we observed notable differences between the two different specimens in stage ii. We further analyzed the signals produced during this phase, as shown in Figure 11. Figure 11A shows the characteristic signal generated by GFRP samples during this phase. From the time–frequency graph of the signal, we can observe that the frequencies of the signal mainly were in the range of 100–200 kHz, indicating that the primary damage feature of the GFRP samples in this phase was still matrix cracking. The peak voltages of Signal1, Signal2, and Signal3 were all above 1×10^{-1} V, with significant increases compared to the values in stage i. From the time-domain graph, we can observe an increase in the amplitude of the signal, with the maximum amplitudes of the three signals exceeding 0.2, 0.5, and 0.5 dB. Moreover, the energy released by the three damage signals was increasing, and both the amplitude and duration of the signal showed an increasing trend. Figure 11B shows the signals produced by the GO-GFRP samples in this phase. Compared to the signals from the GFRP samples in this stage, apart from having the same signal features, it also produced many Signal1-type signals. As shown in the SEM image in Figure 11B, Signal1-type signals were generated due to simultaneous matrix cracking and fiber debonding. The peak frequency range of

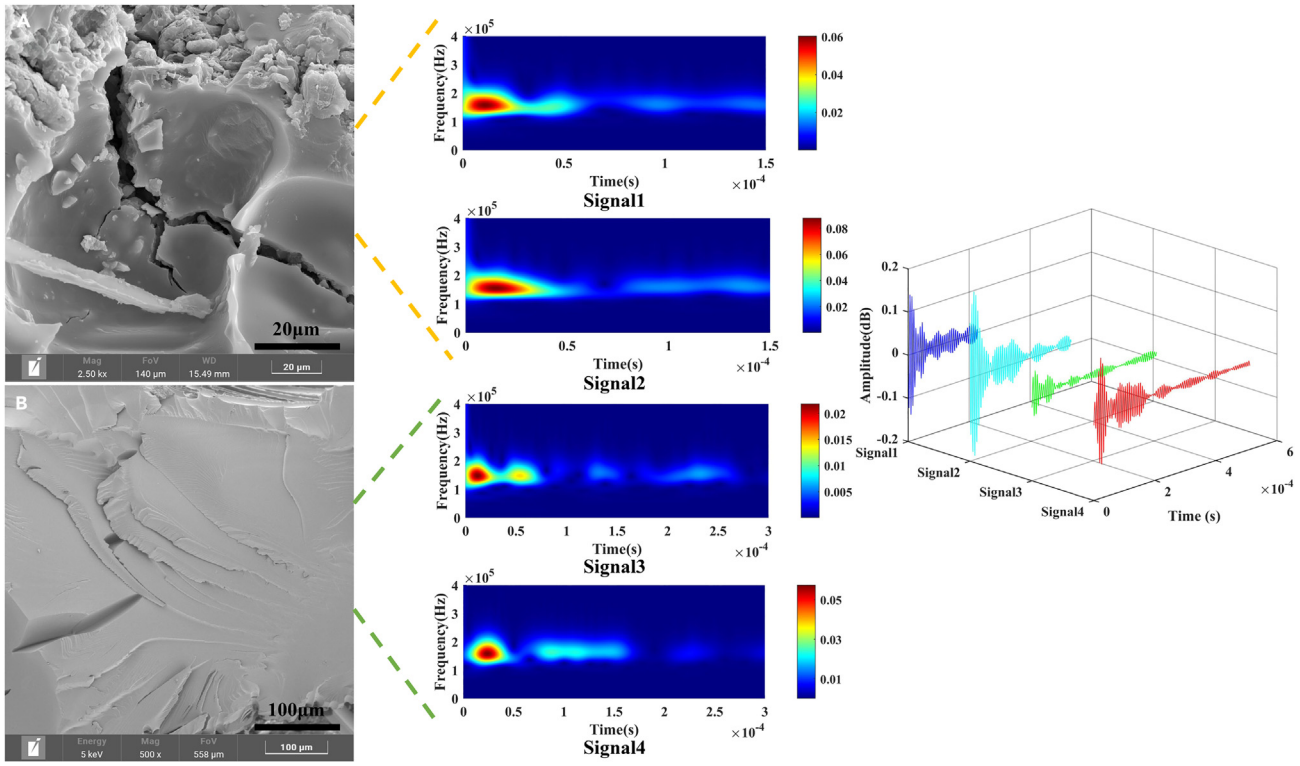

Figure 10. The characteristic signals of GO-GFRP and GFRP samples in stage i

(A) SEM image of matrix cracking in GO-GFRP sample.

(B) SEM image of matrix cracking in GFRP sample.

Signal1 was distributed in the ranges of 100–200 kHz and 200–300 kHz. The frequency range of 200–300 kHz was caused by fiber debonding, as indicated by the orange marking in the SEM image in Figure 11B. However, due to noise interference, this signal also exhibited frequencies exceeding 300 kHz. After decomposing the signal to extract the characteristic signals, we obtained Signal2 and Signal3, with peak frequency ranges of 100–200 kHz and 200–300 kHz, respectively. This suggested that GO-GFRP samples were more prone to fiber debonding than GFRP samples.

Figure 12 shows the characteristic signals of stage iii, which corresponded to the stress failure stage. As shown in Figures 12A–12C, in this stage, all four types of damage (matrix cracking, fiber debonding, delamination, and fiber fracture) occurred simultaneously in both specimens. The amplitudes in the time domain and the voltage values in the time–frequency signals significantly increased. Signal1 corresponded to matrix fiber debonding, and compared to the value of 1×10^{-1} V obtained in the previous stage, the peak voltage reached 1.5 V. The time–domain graph also indicated an amplitude exceeding 3.5 dB. The frequencies of the signals were distributed in the ranges of 100–200 kHz, 200–300 kHz, 300–440 kHz, and 440–625 kHz. Signal2, marked in green in Figure 12A, represents the frequency range of the delamination, which was mainly 300–440 kHz, with a peak voltage of 1.5 V and an amplitude exceeding 3.0 dB. The frequency range of fiber fracture was between 440 and 625 kHz. The orange marker in Figure 12 indicates fiber fracture, resulting in Signal3 and Signal4, with peak amplitudes reaching 10 dB Signal3 represents the fiber fracture caused by multiple fibers. The peak voltage exceeded 6 V, and the time–frequency graph showed that fiber fracture occurred after matrix cracking, fiber debonding, and delamination. To gain a better understanding of the signal distribution range, Signal4 was selected for observation. The red marker indicated intense matrix cracking, accompanied by fiber debonding, delamination, and fiber fracture phenomena under a sustained stress.

DISCUSSION

In this study, a three-point bending damage comparison between GFRP samples with added GO and GFRP samples without added GO was conducted, and the damage evolution process within both materials was observed using AE. The damage to the material during the three-point bending process was divided into three stages (stage i, stage ii, and stage iii) using the sentinel function. The primary differences between GO-GFRP and GFRP samples were observed during stage ii; GO-GFRP samples entered this stage earlier and remained in it for a longer duration. Further analysis and SEM verification of AE characteristic signals were conducted using the MVMD and generalized S transform methods, revealing four types of damage in the materials: matrix cracking, fiber debonding, delamination, and fiber fracture.

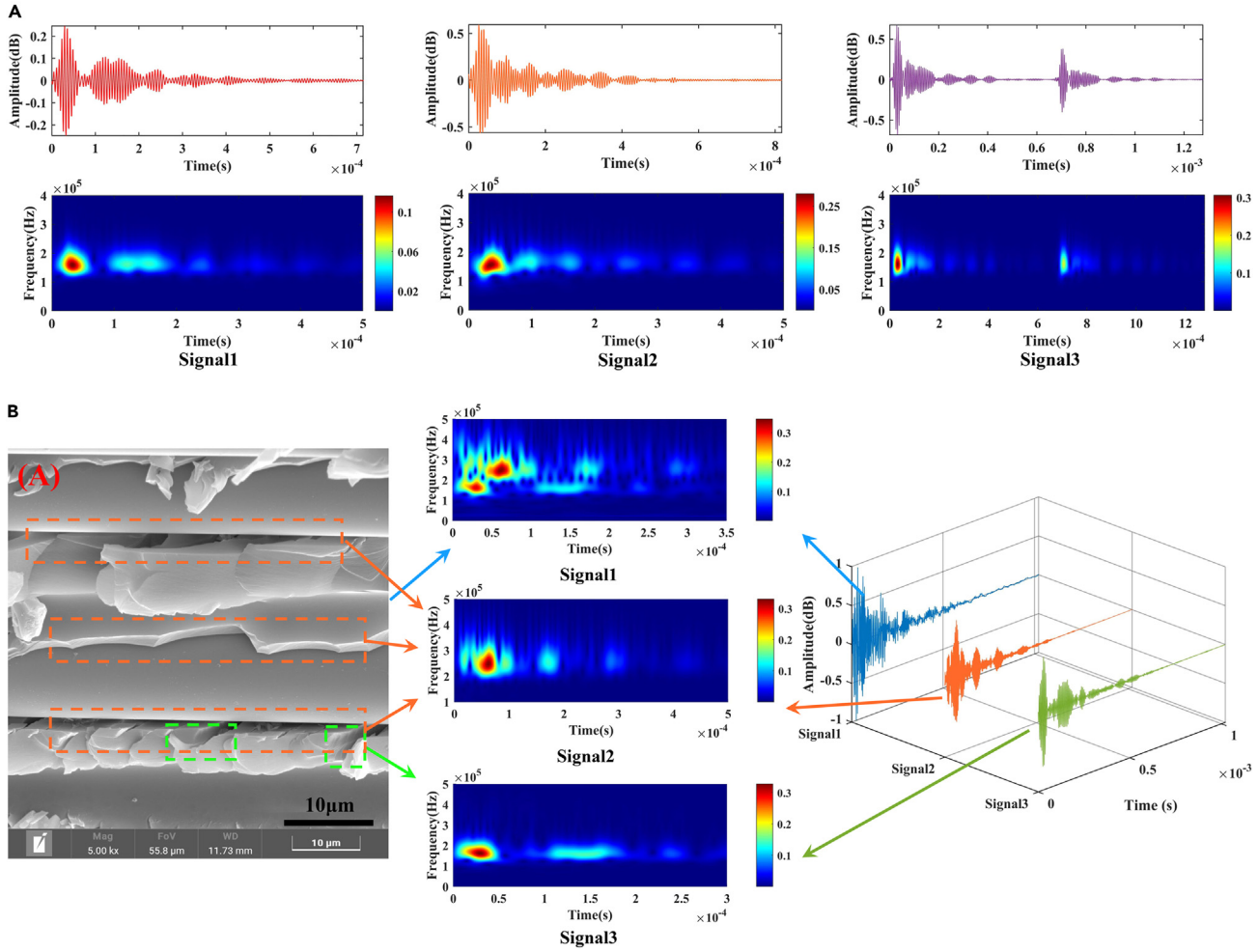

Figure 11. Signals in stage ii

(A) characteristic signal of GFRP samples, (B) damage signal of GO-GFRP samples (the green area corresponds to the characteristic signal of matrix cracking, the orange-red area corresponds to the characteristic signal of fiber debonding, and the characteristic signal corresponding to the SEM damage image is marked with a blue arrow as Signal1).

The corresponding damage frequency ranges were determined to be 100–200 kHz, 200–300 kHz, 300–440 kHz, and 440–625 kHz, respectively. In stage i, the dominant damage mechanism was matrix cracking, with a frequency range of 100–200 kHz for both GFRP and GO-GFRP samples. In stage ii, the primary damage mechanism for GFRP samples remained matrix cracking with a frequency range of 100–200 kHz, while for GO-GFRP samples, the frequency range extended to 100–300 kHz, indicating the occurrence of both matrix cracking and fiber debonding. Stage iii represented the stress transition stage, during which severe matrix cracking, fiber debonding, delamination, and fiber fracture occurred in the specimens.

Limitations of the study

A limitation of this study was that the GO in the utilized materials did not exhibit a gradient distribution.

STAR★METHODS

Detailed methods are provided in the online version of this paper and include the following:

- KEY RESOURCES TABLE
- RESOURCE AVAILABILITY
  - Lead contact
  - Materials availability

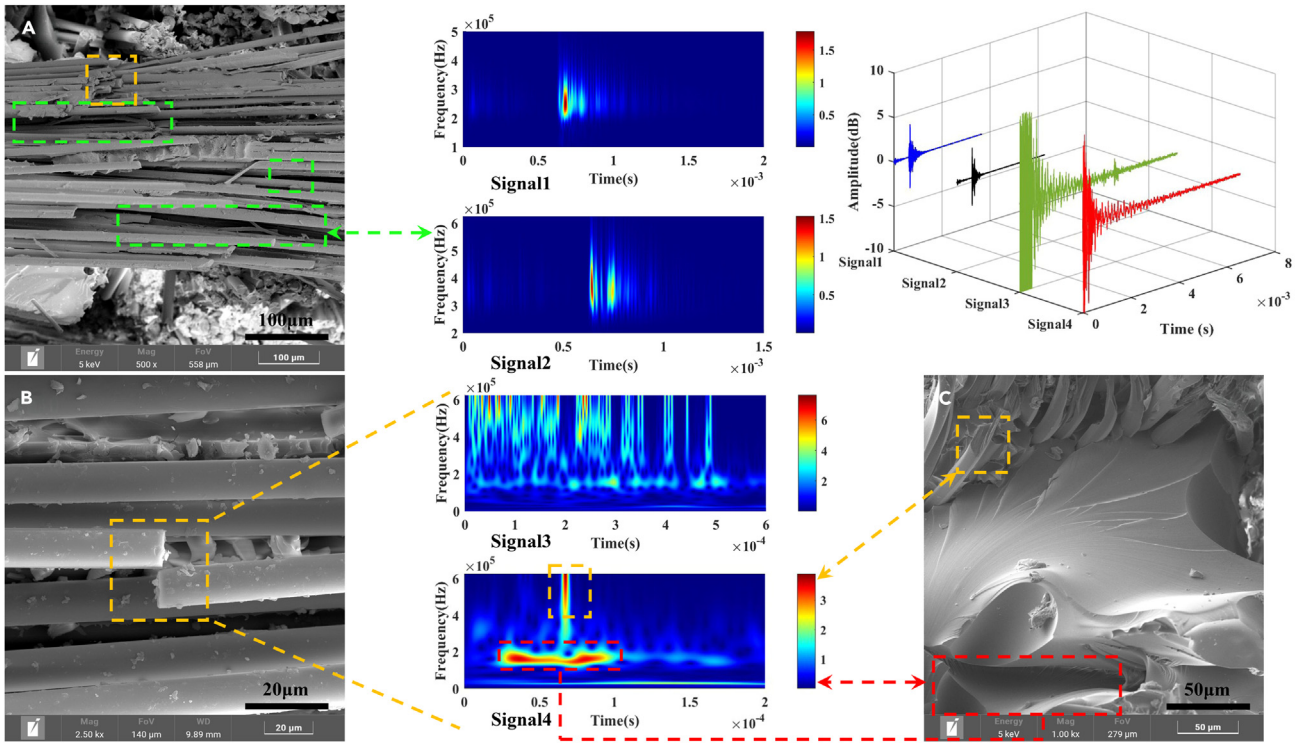

Figure 12. The characteristic signals of GO-GFRP and GFRP samples in stage iii

(A) SEM damage image of fiber fracture and fiber debonding.

(B) SEM image of fiber fracture.

(C) SEM image of fiber fracture and matrix cracking.

ACKNOWLEDGMENTS

This work was financially supported by the Natural Science Foundation of Hunan Province (No. 2021JJ30717), National Natural Science Foundation of China (No.51908064). We thank LetPub (www.letpub.com) for its linguistic assistance during the preparation of this article.

AUTHOR CONTRIBUTIONS

Formal analysis, data curation, supervision, conceptualization, funding acquisition, investigation, methodology, project administration, resources, software, writing – original draft, validation, and writing – review & editing, W.S.; conceptualization, methodology, funding acquisition, resources, data curation, validation, writing – original draft, writing – review & editing, and investigation, L.L.; methodology, resources, validation, and conceptualization, P.Z.; funding acquisition and investigation, B.H.; investigation, W.C.

DECLARATION OF INTERESTS

The authors declare no competing interests.

Received: August 10, 2023
Revised: October 31, 2023
Accepted: November 18, 2023
Published: November 22, 2023

REFERENCES

1. Shahkhosravi, N.A., Yousefi, J., Najafabadi, M.A., Burvill, C., and Minak, G. (2019). Fatigue life reduction of GFRP composites due to delamination associated with the introduction of functional discontinuities. Compos. B Eng. *163*, 536–547.
2. Verma, L., Andrew, J.J., Sivakumar, S.M., Balaganesan, G., Vedantam, S., and Dhakal, H.N. (2021). Evaluation of quasi-static indentation response of superelastic shape memory alloy embedded GFRP laminates using AE monitoring. Polym. Test. *93*, 106942.
3. He, H., Chen, W., Luo, B., Bian, K., Xiang, N., Yin, Y., Zhang, Z., Dai, M., and He, T. (2022). On the electrical breakdown of GFRP wind turbine blades due to direct lightning strokes. Renew. Energy *186*, 974–985.
4. Wang, P., Ke, L.-Y.-W., Wu, H.-L., Leung, C.K., and Li, W.-W. (2023). Hygrothermal aging effects on the diffusion-degradation process of GFRP composite: Experimental study and numerical simulation. Constr. Build. Mater. *379*, 131075.
5. Hofmann, M., Shahid, A.T., Machado, M., Garrido, M., Bordado, J.C., and Correia, J.R. (2022). GFRP biocomposites produced with a novel high-performance bio-based unsaturated polyester resin. Compos. Part A Appl. Sci. Manuf. *161*, 107098.
6. Das, S., Halder, S., Khan, N.I., Paul, B., and Goyat, M.S. (2020). Assessing damage mitigation by silanized milled graphite nanoparticles in hybrid GFRP laminated composites. Compos. Part A Appl. Sci. Manuf. *132*, 105784.
7. Zamani, P., Fm da Silva, L., Masoudi Nejad, R., Ghahremani Moghaddam, D., and Soltannia, B. (2022). Experimental study on mixing ratio effect of hybrid graphene nanoplatelet/nano-silica reinforcement on the static and fatigue life of aluminum-to-GFRP bonded joints under four-point bending. Compos. Struct. *300*, 116108.
8. Xie, H., Cao, T., Rodríguez-Lozano, F.J., Luong-Van, E.K., and Rosa, V. (2017). Graphene for the development of the next-generation of biocomposites for dental and medical applications. Dent. Mater. *33*, 765–774.
9. Sari, F., and Ugurlu, M. (2023). Reinforcement of resin-modified glass-ionomer cement with glass fiber and graphene oxide. J. Mech. Behav. Biomed. Mater. *142*, 105850.
10. Fu, X., Lin, J., Liang, Z., Yao, R., Wu, W., Fang, Z., Zou, W., Wu, Z., Ning, H., and Peng, J. (2023). Graphene oxide as a promising nanofiller for polymer composite. Surf. Interfaces *37*, 102747.
11. Chen, L., Shen, Y., Yi, H., Liu, Z., and Song, Q. (2021). Mathematical modeling of heat transfer in GO-doped reinforce polymer for anti-/deicing of wind turbines. Int. Commun. Heat Mass Transf. *123*, 105235.
12. Zhao, J., Zhang, S., Ke, X., Pan, A., Zhou, Q., Zeng, S., Chen, P., Xu, Y., Nie, W., and Zhou, Y. (2023). Simultaneously tuning interfacial and interlaminar properties of glass fiber fabric/epoxy laminated composites via modifying fibers with graphene oxide. Compos. Sci. Technol. *235*, 109970.
13. García Márquez, F.P., and Peco Chacón, A.M. (2020). A review of non-destructive testing on wind turbines blades. Renew. Energy *161*, 998–1010.
14. Gholizadeh, S., Leman, Z., and Baharudin, B.T.H.T. (2023). State-of-the-art ensemble learning and unsupervised learning in fatigue crack recognition of glass fiber reinforced polyester composite (GFRP) using acoustic emission. Ultrasonics *132*, 106998.
15. Jung, D., Yu, W.-R., Ahn, H., and Na, W. (2022). New b-value parameter for quantitatively monitoring the structural health of carbon fiber-reinforced composites. Mech. Syst. Signal Process. *165*, 108328.
16. Friedrich, L., Colpo, A., Maggi, A., Becker, T., Lacidogna, G., and Iturrioz, I. (2021). Damage process in glass fiber reinforced polymer specimens using acoustic emission technique with low frequency acquisition. Compos. Struct. *256*, 113105.
17. Yang, J., Zhao, K., Yu, X., Yan, Y., He, Z., Zhou, Y., and Lai, Y. (2022). Fracture evolution of fiber-reinforced backfill based on acoustic emission fractal dimension and b-value. Cem. Concr. Compos. *134*, 104739.
18. Jung, D., Lee, B.-S., Yu, W.-R., and Na, W. (2021). Effect of propagation distance on acoustic emission of carbon fiber/epoxy composites. Struct. Health Monit. *20*, 3342–3353.
19. Wang, X., Xie, H., Tong, Y., Wang, B., and Hu, H. (2023). Three-point bending properties of 3D_C/C_TiC_Cu composites based on acoustic emission technology. Mech. Syst. Signal Process. *184*, 109693.
20. Zhang, Y., Zhou, B., Yu, F., and Chen, C. (2021). Cluster analysis of acoustic emission signals and infrared thermography for defect evolution analysis of glass/epoxy composites. Infrared Phys. Technol. *112*, 103581.
21. Harizi, W., Chaki, S., Bourse, G., and Ourak, M. (2022). Damage mechanisms assessment of Glass Fiber-Reinforced Polymer (GFRP) composites using multivariable analysis methods applied to acoustic emission data. Compos. Struct. *289*, 115470.
22. Mi, Y., Zhu, C., Li, X., and Wu, D. (2020). Acoustic emission study of effect of fiber weaving on properties of fiber-resin composite materials. Compos. Struct. *237*, 111906.
23. Azadi, M., Sayar, H., Ghasemi-Ghalebahman, A., and Jafari, S.M. (2019). Tensile loading rate effect on mechanical properties and failure mechanisms in open-hole carbon fiber reinforced polymer composites by acoustic emission approach. Compos. B Eng. *158*, 448–458.
24. Chelliah, S.K., Parameswaran, P., Ramasamy, S., Vellayaraj, A., and Subramanian, S. (2019). Optimization of acoustic emission parameters to discriminate failure modes in glass–epoxy composite laminates using pattern recognition. Struct. Health Monit. *18*, 1253–1267.
25. Beheshtizadeh, N., Mostafapour, A., and Davoodi, S. (2019). Three point bending test of glass/epoxy composite health monitoring by acoustic emission. Alexandria Eng. J. *58*, 567–578.
26. Bakhtiary Davijani, A.A., Hajikhani, M., and Ahmadi, M. (2011). Acoustic Emission based on sentry function to monitor the initiation of delamination in composite materials. Mater. Des. *32*, 3059–3065.
27. Barile, C., Casavola, C., Pappalettera, G., and Vimalathithan, P.K. (2019). Damage characterization in composite materials using acoustic emission signal-based and parameter-based data. Compos. B Eng. *178*, 107469.
28. Rehman, N.U., and Aftab, H. (2019). Multivariate variational mode decomposition. IEEE Trans. Signal Process. *67*, 6039–6052.
29. Stockwell, R.G., Mansinha, L., and Lowe, R.P. (1996). Localization of the complex spectrum: The S transform. IEEE Trans. Signal Process. *44*, 998–1001.
30. Hoseinlaghab, S., Farahani, M., Safarabadi, M., and Nikkhah, M. (2023). Tension-after-impact analysis and damage mechanism evaluation in laminated composites using AE monitoring. Mech. Syst. Signal Process. *186*, 109844.
31. Zhao, W.-Z., and Zhou, W. (2019). Cluster analysis of acoustic emission signals and tensile properties of carbon/glass fiber–reinforced hybrid composites. Struct. Health Monit. *18*, 1686–1697.

STAR★METHODS

KEY RESOURCES TABLE

REAGENT or RESOURCE	SOURCE	IDENTIFIER
Deposited data		
Raw data	Lida Liao	https://www.csust.edu.cn/ndxy/info/1434/9048.htm
Software and algorithms		
MATLAB 2023a	MathWorks	https://ww2.mathworks.cn/
Origin.8	OriginLab	http://www.OriginLab.com

RESOURCE AVAILABILITY

Lead contact

Further information can be requested via the lead contact, Lida Liao (lidaliao@csust.edu.cn).

Materials availability

This study did not generate any new reagents.

Data and code availability

- All data reported in this paper will be shared by the lead contact upon request.
- This paper did not produce any new code.
- Any additional information related to this paper can be provided by the main contact upon request.

EXPERIMENTAL MODEL AND SUBJECT DETAILS

Materials and methods

The GFRP and GO-GFRP composite laminates were prepared using two layers of unidirectional glass fiber cloth. The following was the preparation method for this material: First, the cut unidirectional glass fiber cloth was laid on a flat mold, followed by placing 1 layer of release fabric and 2 layers of glass fiber cloth. Next, epoxy resin, hardener, and graphene oxide were mixed in a ratio of 100 g of epoxy resin, 34 g of hardener, and 5 g of graphene oxide, and they were blended evenly through mechanical stirring. Afterward, the mixed material was poured into the glass fiber cloth to ensure complete impregnation and bubble removal, and another layer of release fabric was added on top, laminating it to the desired thickness. The laminated board was then heated on a heating platform at 70°C and was cured under pressure for 4 h. After curing, it was placed in a vacuum drying oven set to 60°C and was dried for 24 h. In the drying oven, it cured into an epoxy resin-glass fiber composite laminate. To ensure the effectiveness of the composite laminate sample, the air conditioning was adjusted to room temperature and the doors and windows were closed. Finally, in order to minimize internal damage to the sample during the cutting process and to prevent excessive heat generation that might even burn the sample, a water cutting method was used to cut the GFRP composite pressure plate.

METHOD DETAILS

Material characterization

The EDS, FTIR, XPS, and SEM tests in this paper were conducted with the support and assistance of Hunan Navi NewMaterials Technology.

AE testing procedure for materials

Before the official experiment began, the sensitivity of the entire acoustic emission (AE) collection system was tested using AE sensors to determine if the collection system met the acquisition requirements. In this study, the lead breakage method was used to test the system's sensitivity. First, the load application location was identified at the center of the GFRP specimen. A fixed point was taken in the middle of the load application location as a marker, which served as the AE source for the lead breakage signal. Next, markers were drawn at distances of 3 cm, 5 cm, and 7 cm from the AE source of the lead breakage signal, all located on the specimen. The sensor received the lead breakage AE signal ten times at each of these positions. If the maximum amplitude difference of the received signal at the same position did not exceed 3 dB and the AE amplitude was greater than 90 dB, it was considered that the overall sensitivity of the AE system met the experimental requirements at that position. The breakage length of the automatic pencil lead was uniformly set to 5 mm, with the angle between the pencil

lead and the horizontal plane of the specimen being 30°. After a total of 30 lead breakages, the results were as shown in the table below. It can be seen that the system's accuracy met the experimental requirements at all three positions. As the distance between the sensor and the AE source of the lead breakage increased, there was a certain attenuation in the AE signal amplitude.

QUANTIFICATION AND STATISTICAL ANALYSIS

No statistical analysis is used.